

# SPIRiT: Iterative Self-consistent Parallel Imaging Reconstruction From Arbitrary $k$ -Space

Michael Lustig<sup>1,2\*</sup> and John M. Pauly<sup>2</sup>

**A new approach to autocalibrating, coil-by-coil parallel imaging reconstruction, is presented. It is a generalized reconstruction framework based on self-consistency. The reconstruction problem is formulated as an optimization that yields the most consistent solution with the calibration and acquisition data. The approach is general and can accurately reconstruct images from arbitrary  $k$ -space sampling patterns. The formulation can flexibly incorporate additional image priors such as off-resonance correction and regularization terms that appear in compressed sensing. Several iterative strategies to solve the posed reconstruction problem in both image and  $k$ -space domain are presented. These are based on a projection over convex sets and conjugate gradient algorithms. Phantom and in vivo studies demonstrate efficient reconstructions from undersampled Cartesian and spiral trajectories. Reconstructions that include off-resonance correction and nonlinear  $\ell_1$ -wavelet regularization are also demonstrated. Magn Reson Med 64:457–471, 2010. © 2010 Wiley-Liss, Inc.**

**Key words:** image reconstruction; autocalibration; parallel imaging; compressed sensing; SENSE; GRAPPA; iterative reconstruction

Multiple receiver coils have been used since the beginning of MRI (1), mostly for the benefit of increased signal-to-noise ratio. In the late 1980's, Kelton et al. (2) proposed in an abstract to use multiple receivers for scan acceleration. However, it was not until the late 1990s when Sodickson and Manning (3) presented their method simultaneous acquisition of spatial harmonics (SMASH) and later Pruessmann et al. (4) presented SENSE, that accelerated scans using multiple receivers became a practical and viable option.

Multiple receiver coil scans can be accelerated because the data obtained for each coil are acquired in parallel and each coil image is weighted differently by the spatial sensitivity of its coil. This sensitivity information in conjunction with gradient encoding reduces the required number of data samples that are needed for reconstruction. This concept of reduced data acquisition by combined sensitivity and gradient encoding is widely known as parallel imaging.

Over the years, a variety of methods for parallel imaging reconstruction has been developed. These methods differ

by the way the sensitivity information is used. Methods like SMASH (3), sensitivity encoding (SENSE) (4,5), sensitivity profiles from an array of coils for encoding and reconstruction in parallel (SPACE-RIP) (6), parallel magnetic resonance imaging with adaptive radius in  $k$ -space (PARS) (7), and parallel imaging reconstruction for arbitrary trajectories using  $k$ -space sparse matrices (kSPA) (8) explicitly require the coil sensitivities to be known. In practice, it is very difficult to measure the coil sensitivities with high accuracy. Errors in the sensitivity are often amplified and even small errors can result in visible artifacts in the image (9). On the other hand, autocalibrating methods like auto-SMASH (10,11), partially parallel imaging with localized sensitivities (PILS) (12), generalized autocalibrating partially parallel acquisitions (GRAPPA) (13), and anti-aliasing partially parallel encoded acquisition reconstruction (APPEAR) (14) implicitly use the sensitivity information for reconstruction and avoid some of the difficulties associated with explicit estimation of the sensitivities. Another major difference is in the reconstruction target. SMASH, SENSE, SPACE-RIP, kSPA, and AUTO-SMASH attempt to directly reconstruct a single combined image. Coil-by-coil methods, PILS, PARS, and GRAPPA directly reconstruct the individual coil images, leaving the choice of combination to the user. In practice, coil-by-coil methods tend to be more robust to inaccuracies in the sensitivity estimation and often exhibit fewer visible artifacts (9,14,15).

SENSE is an explicit sensitivity-based, single-image reconstruction method. Among all methods, the SENSE approach is the most general. It provides a framework for reconstruction from arbitrary  $k$ -space sampling and to easily incorporate additional image priors. When the sensitivities are known, SENSE is the optimal solution (14,15). To the best of the authors' knowledge, none of the coil-by-coil autocalibrating methods are as flexible and optimal as SENSE. Some proposed methods (16–19) adapt GRAPPA to reconstruct some non-Cartesian trajectories, but these require approximations and therefore lose some of the ability to remove all the aliasing artifacts.

Here, we propose a new approach to parallel imaging reconstruction called SPIRiT (iterative self-consistent parallel imaging reconstruction). It is a coil-by-coil autocalibrating reconstruction. It is heavily based on the GRAPPA reconstruction but also draws its inspiration from SENSE in the sense that the reconstruction is formulated as an inverse problem in a very general way. The result is that the reconstruction is the solution for a least-squares optimization. SPIRiT is based on self-consistency with the calibration and acquisition data. It is flexible and can reconstruct data from arbitrary  $k$ -space sampling patterns and easily incorporates additional image priors.

<sup>1</sup>Department of Electrical Engineering and Computer Science, University of California at Berkeley, Berkeley, California, USA

<sup>2</sup>Magnetic Resonance Systems Research Laboratory, Department of Electrical Engineering, Stanford University, Stanford, California, USA

Grant sponsor: NIH; Grant numbers: P41RR09784, R01EB007588, and R21EB007715.

\*Correspondence to: Michael Lustig, Ph.D., 506 Cory Hall, University of California, Berkeley, Berkeley, CA 94720. E-mail: mlustig@eecs.berkeley.edu  
Received 13 January 2010; revised 13 January 2010; accepted 11 February 2010.

DOI 10.1002/mrm.22428

Published online in Wiley InterScience (www.interscience.wiley.com).

In this paper, we first review the foundations of SPIRiT, e.g., the GRAPPA method. We then define the SPIRiT consistency constraints and show that the reconstruction is a solution to an optimization problem. We then extend the method to arbitrary sampling patterns with  $k$ -space-based and image-based approaches. Finally, we show that the method can easily introduce additional priors such as off-resonance correction and regularization.

## CARTESIAN GRAPPA

The GRAPPA reconstruction poses the parallel imaging reconstruction as a *translation variant* interpolation problem in  $k$ -space. It is a self-calibrating coil-by-coil reconstruction method. Unlike SENSE, which attempts to reconstruct a single combined image, GRAPPA attempts to reconstruct the individual coil images directly.

In the traditional GRAPPA (13) algorithm a *nonacquired*  $k$ -space value in the  $i$ th coil, at position  $r$ ,  $x_i(r)$ , is synthesized by a linear combination of acquired neighboring  $k$ -space data from all coils. Let  $R_r$  be a set of operators that choose points from a single-coil Cartesian  $k$ -space, such that the product  $R_r x_j$  is a vector containing the  $k$ -space points in the neighborhood of position  $r$ . Let  $\tilde{R}_r$  be the operators that choose a smaller subset of only the *acquired*  $k$ -space locations in the neighborhood of position  $r$ . The recovery of  $x_i(r)$  is given by:

$$x_i(r) = \sum_j g_{rji}^* (\tilde{R}_r x_j), \quad [1]$$

where  $g_{rji}$  is a vector set of weights obtained by calibration for the particular sampling pattern around position  $r$ , and  $g_{rji}^*$  is its transpose-conjugate. The full  $k$ -space grid is reconstructed by solving Eq. 1 for each unacquired  $k$ -space in all coils and all positions.

The linear combination weights, or calibration kernel, used in Eq. 1 are obtained by calibration from a fully acquired  $k$ -space region. The calibration finds the set of weights that is the most consistent with the calibration data in the least-squares sense. In other words, the calibration stage looks for a set of weights such that if one tries to synthesize each of the calibration points from its neighborhood, the result should be as close as possible to the true calibration points. More formally, the calibration is described by the following equation:

$$\underset{g_{ri}}{\operatorname{argmin}} \sum_{\rho \in \text{Calib}} \left\| \sum_j g_{rji}^* (\tilde{R}_\rho x_j) - x_i(\rho) \right\|^2, \quad [2]$$

where  $g_{ri}$  is a concatenation of all  $g_{rji}$ 's or,  $g_{ri} = [g_{r1i}, g_{r2i}, \dots, g_{rNi}]^T$ . The above can be written in matrix form as:

$$\underset{g_{ri}}{\operatorname{argmin}} \left\| \tilde{X}^* g_{ri} - x_i \right\|^2, \quad [3]$$

in which the entries of  $\tilde{X}$  are all the  $\tilde{R}_r x_i$  vectors in the calibration area of  $k$ -space that were reordered into a matrix. This equation is often solved as Tikhonov regularized least-squares, which has the analytic solution:

$$g_{ri} = (\tilde{X}^* \tilde{X} + \beta I)^{-1} \tilde{X}^* x_i. \quad [4]$$

The assumption is that if the calibration consistency holds within the calibration area, it also holds in other parts of  $k$ -space. Therefore, Eq. 1 can be used for the reconstruction. In the original GRAPPA paper, the undersampling pattern was such that the  $k$ -space sampling in the neighborhood of the missing points is the same for all points. Therefore, a single set of weights is enough for reconstruction and the calibration can be performed only once. In two-dimensional (2D) acceleration, however, the sampling pattern around each missing point can be quite different. Different sets of weights must be obtained for each sampling pattern. As an illustration, consider the 2D GRAPPA reconstruction in Fig. 1a. The figure portrays two equations to solve two missing data points. Each of the equations uses a different set of calibration weights. The neighborhood size in that example for illustration purposes is a square of three  $k$ -space pixels.

## MATERIALS AND METHODS

### SPIRiT: A Self-consistency Formulation

Inspired by GRAPPA, we take on a slightly different approach that has similar properties to GRAPPA but is more general and uses the data more efficiently. Our aim is to describe the reconstruction as an inverse problem governed by data consistency constraints. The key in the approach is to separate the consistency constraints into (a) consistency with the calibration, and (b) consistency with the data acquisition. We formulate these constraints as sets of linear equations. The desired reconstruction is the solution that satisfies the sets of equations best according to a suitable error measure criterion.

Even though the acquired  $k$ -space data may or may not be Cartesian, ultimately, the desired reconstruction is a complete Cartesian  $k$ -space grid for each of the coils. Therefore, we define the entire Cartesian  $k$ -space grid for all the coils as the unknown variables in the equations. This step makes the formulation very general, especially when considering noisy data, regularization, and non-Cartesian sampling.

### Consistency With the Calibration

Traditional GRAPPA enforces calibration consistency only between synthesized points and the acquired points in their associated neighborhoods. The proposed approach expands the notion of consistency by enforcing consistency between every point on the grid,  $x_i(r)$ , and its entire neighborhood across all coils (*e.g.*,  $R_r x_j$ ). It is important to emphasize that the notion *entire neighborhood* includes all the  $k$ -space points near  $x_i(r)$  in all coils, whether they were acquired or not. Given the above, the consistency equation for *all*  $k$ -space positions is given by,

$$x_i(r) = \sum_j g_{ji}^* (R_r x_j). \quad [5]$$

The difference between  $g_{ji}$  here and the traditional GRAPPA weights  $g_{rji}$  in Eq. 1, is that  $g_{ji}$  is a full kernel independent of the actual  $k$ -space sampling pattern and is the same for

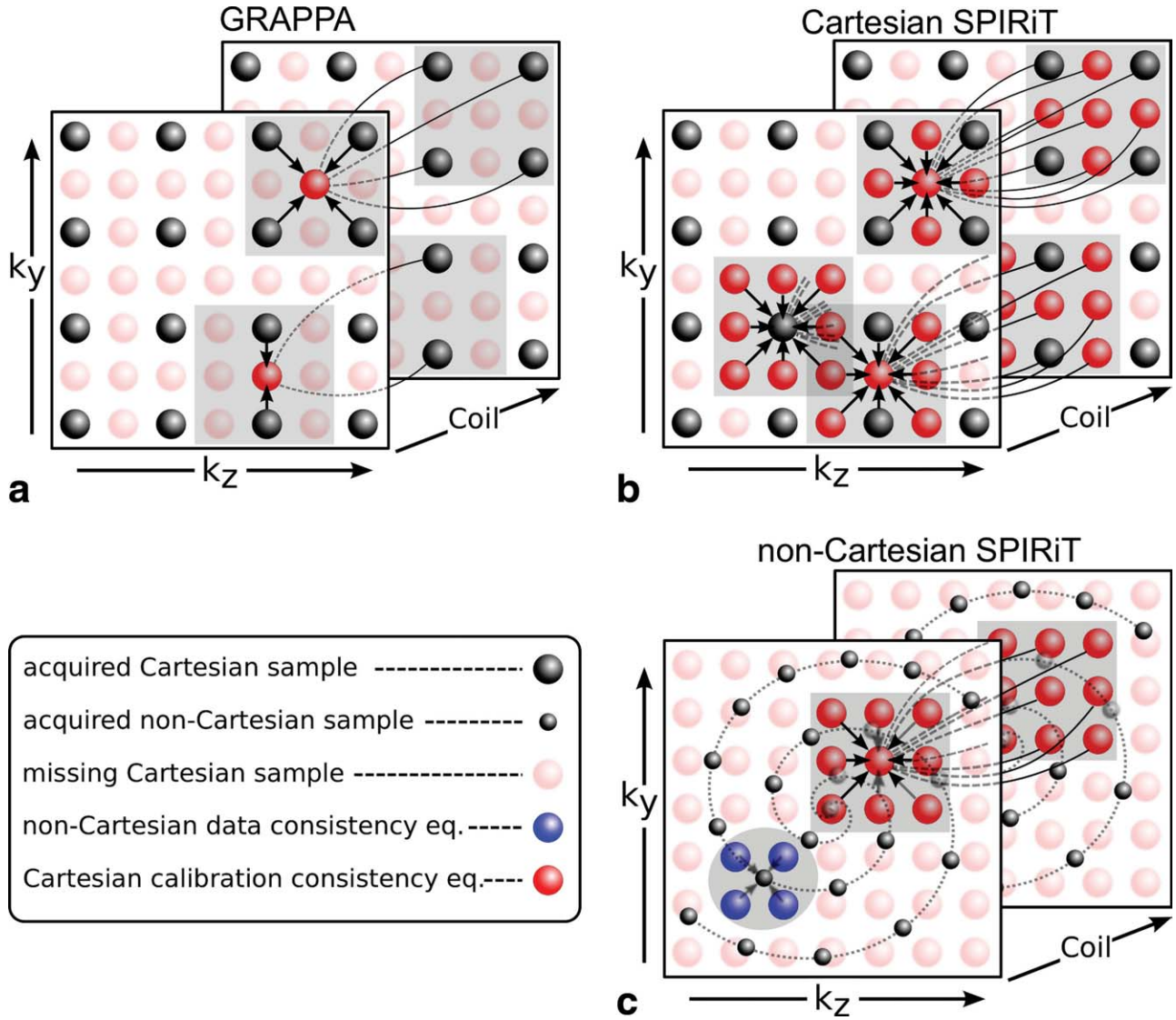


FIG. 1. **a:** Traditional 2D GRAPPA. Missing  $k$ -space data are synthesized from neighboring acquired data. The synthesizing kernel depends on the specific sampling pattern in the neighborhood of the missing point. The reconstruction of a point is independent of the reconstruction of other missing points. **b:** Cartesian SPIRiT reconstruction. Three consistency equations are illustrated. The reconstruction of each point on the grid is dependent on its entire neighborhood. The reconstruction of missing points depends on the reconstruction of other missing points. The calibration consistency equation is independent of the sampling pattern. **c:** Non-Cartesian SPIRiT. The calibration consistency equation is Cartesian (red). The acquisition data consistency relation between the Cartesian missing points and the non-Cartesian acquired points is shown in blue. These define a large set of linear equations that is sufficient for reconstruction.

all  $k$ -space positions. It is obtained by using the operators  $R_r$  instead of  $\tilde{R}_r$  in Eq. 2. Equation 1 defines a large set of *decoupled* linear equations that can be solved separately. On the other hand, Eq. 5 defines a large set of *coupled* linear equations. As an illustration, consider Fig. 1b, which has a sampling setup similar to that of the 2D GRAPPA problem in Fig. 1a. In the figure, three equations are portrayed. It shows that the synthesis of a missing central point depends on both acquired and missing points in its neighborhood and that the equations are coupled.

It is convenient to write the entire coupled system of equations in matrix form. Let  $x$  be the entire  $k$ -space grid data for all coils, and let  $G$  be a matrix containing the  $g_{ji}$ 's in the appropriate locations. The system of equations can simply be written as,

$$x = Gx. \quad [6]$$

The matrix  $G$  is in fact a series of convolution operators (denoted as  $a \otimes b$ ) that convolve the entire  $k$ -space with the appropriate calibration kernels,

$$x_i = \sum_j g_{ij} \otimes x_j. \quad [7]$$

Equations 6–7 can be explained intuitively. Applying the operation  $G$  on  $x$  is the same as attempting to synthesize every point from its neighborhood. If  $x$  is indeed the correct solution, then synthesizing every point from its neighborhood should yield exactly the same  $k$ -space data!

### Consistency With the Data Acquisition

Of course, any plausible reconstruction has to be consistent with the real data that were acquired by the scanner. This constraint can also be expressed as a set of linear equations in matrix form. Let  $y$  be the vector of acquired data from all coils (concatenated). Let the operator  $D$  be a linear operator that relates the reconstructed Cartesian  $k$ -space,  $x$ , to the acquired data. The data acquisition consistency is given by

$$y = Dx. \quad [8]$$

This formulation is very general in the sense that  $x$  is always Cartesian  $k$ -space data, whereas  $y$  can be data acquired with arbitrary  $k$ -space sampling patterns. In Cartesian acquisitions, the operator  $D$  selects only acquired  $k$ -space locations. The selection can be arbitrary: uniform, variable density, or pseudorandom patterns. In non-Cartesian sampling, the operator  $D$  represents an interpolation matrix. It interpolates data from a Cartesian  $k$ -space grid onto non-Cartesian  $k$ -space locations in which the data were acquired.

### Constrained Optimization Formulation

Equations 6 and 8 describe the calibration and data acquisition consistency constraints as sets of linear equations that the reconstruction must satisfy. However, due to noise and calibration errors these equations can only be solved approximately. Therefore, we propose as reconstruction the solution to an optimization problem given by,

$$\begin{aligned} \text{minimize} \quad & \| (G - I)x \|^2 \\ \text{s.t.} \quad & \| Dx - y \|^2 \leq \epsilon. \end{aligned} \quad [9]$$

The parameter  $\epsilon$  is introduced as a way to control the consistency. It trades off data acquisition consistency with calibration consistency. The beauty in this formulation is that the calibration consistency is always applied to a Cartesian  $k$ -space, even though the acquired data may be non-Cartesian. The treatment of non-Cartesian sampling appears only in the data acquisition constraint. This is illustrated more clearly in Fig. 1c.

A useful reformulation of Eq. 9 is the unconstrained Lagrangian form,

$$\arg\min_x \| Dx - y \|^2 + \lambda(\epsilon) \| (G - I)x \|^2. \quad [10]$$

As is well known, the parameter  $\lambda$  can be chosen appropriately such that the solution of Eq. 10 is exactly as Eq. 9. In general, the optimization in Eqs. 9–10 and variations of it can often be solved very efficiently by iterative descent methods such as steepest descent or the much more efficient conjugate gradient (CG) algorithm. These are all based on the ability to rapidly calculate the gradient of the objective function which is,

$$\begin{aligned} \nabla_x \{ \| Dx - y \|^2 + \lambda \| (G - I)x \|^2 \} \\ = 2D^*(Dx - y) + \lambda 2(G - I)^*(G - I)x. \end{aligned} \quad [11]$$

A steepest descent algorithm with a step size  $\mu$  would simply calculate

$$x_{n+1} = x_n - \mu [D^*(Dx - y) + \lambda(G - I)^*(G - I)x]$$

Table 1  
A POCS Algorithm for SPIRiT From Arbitrary Sampling on a Cartesian Grid

POCS SPIRiT Cartesian Reconstruction	
Inputs:	$y$ - $k$ -space measurements from all coils $D$ - operator selecting acquired $k$ -space $D_c$ - operator selecting nonacquired $k$ -space $G$ - SPIRiT operator matrix obtained from calibration $\text{errTol}$ - stopping tolerance
Outputs:	$x_k$ - reconstructed $k$ -space for all coils
Algorithm:	$x_0 = D^T y$ ; $k = 0$ do { $k = k + 1$ $x_k = Gx_{k-1}$ % calibration consistency projection $x_k = D_c^T D_c x_k + D^T y$ % data acquisition consistency projection $e = \ x_k - x_{k-1}\ $ % Error stopping criteria $x_{k-1} = x_k$ }while $e > \text{errTol}$

at every iteration. It is fortunate that in the cases discussed in this paper, both the  $G$  and  $D$  operation and their adjoints  $G^*$  and  $D^*$  can be calculated very quickly. In the next sections, we will provide the reconstruction details for more specific examples, including the calculation of the  $G$  and  $D$  operators and their adjoints.

### Arbitrary Cartesian Sampling

In some cases, it may be useful to leave the acquired  $k$ -space unchanged. This is equivalent to enforcing data acquisition equality constraint (*i.e.*,  $\epsilon \rightarrow 0$  in Eq. 9). One way to implement this is through continuation by starting with a large value of  $\lambda$  and then iteratively reducing it while repeatedly solving Eq. 10. A simpler and more efficient approach is to incorporate the equality constraint in the objective, such that the problem is formulated as simple least squares. Let  $y$  be the vector of acquired points, let  $\tilde{x}$  now be the vector representing only the missing points, and let  $D$  and  $D_c$  be the matrices that select the acquired and nonacquired points out of the full  $k$ -space grid respectively. This way,  $D^T$  and  $D_c^T$  take the selected acquired and nonacquired samples and put them back in the right location in the full  $k$ -space grid. We can now write  $x$  as  $x = D^T y + D_c^T \tilde{x}$ . Substituting into Eq. 9 we get,

$$\begin{aligned} \arg\min_{\tilde{x}} \| Dx - y \|^2 + \lambda \| (G - I)x \|^2 \\ = \arg\min_{\tilde{x}} \| D(D^T y + D_c^T \tilde{x}) - y \|^2 + \lambda \| (G - I)(D^T y + D_c^T \tilde{x}) \|^2 \\ = \arg\min_{\tilde{x}} \| y + 0 - y \|^2 + \lambda \| (G - I)D_c^T \tilde{x} + (G - I)D^T y \|^2 \\ = \arg\min_{\tilde{x}} \| (G - I)D_c^T \tilde{x} + (G - I)D^T y \|^2, \end{aligned} \quad [12]$$

which has the usual format of a least-norm-least-squares problem, *e.g.*,  $\arg\min_x \| Ax - b \|^2$ , where  $A = (G - I)D_c^T$  and  $b = -(G - I)D^T y$ . This can be solved directly using sparse matrices or iteratively using standard descent algorithms like CG. Another efficient alternative is to find a solution for  $Gx = x$ , using a projection over convex sets (POCS) algorithm. The POCS approach is described in Table 1.

### Non-Cartesian Sampling

In theory, Eq. 9 is the solution for the non-Cartesian case. However, the practical success of the reconstruction depends on how well the operators  $G$  and  $D$  approximate the true data and how fast they can be computed in practice. The main difficulty facing the reconstruction is an accurate and efficient interpolation scheme in  $k$ -space. Next, we present two approaches. The first operates entirely in  $k$ -space. The other also applies calculations in the image domain.

### Calibration

The SPIRiT approach is autocalibrating. We assume that there is always a subset of  $k$ -space that is sufficiently sampled for the purpose of calibration. For example, radial trajectories and dual density spiral (18) trajectories have a region around the  $k$ -space origin that is sufficiently sampled. From such data, Cartesian calibration data are obtained by interpolation. Alternatively, such a Cartesian calibration region can be obtained by a separate scan. The full kernel weights are calculated from calibration data similar to Eq. 4.

### $k$ -Space Domain Reconstruction

The most natural way to approximate the data consistency constraint  $y = Dx$  is to use convolution interpolation to interpolate from Cartesian onto the non-Cartesian  $k$ -space grid and vice versa. This is very similar to the gridding algorithm. However, several details need to be taken into consideration.

Consider a convolution interpolation of the  $i$ th coil's  $k$ -space data from a Cartesian grid to a non-Cartesian grid. Let  $c$  be an interpolation kernel,  $k$  be the non-Cartesian  $k$ -space coordinates, and  $\delta(x)$  the usual impulse function. One can write the operation  $D$  applied to the  $i$ th coil's data as,

$$y_i(n) = \int_r \delta(k(n) - r) \{c * x_i\}(r) dr \quad [13]$$

Ideally, the interpolation kernel,  $c$ , should be a sinc function. However, this has a prohibitively large kernel size. Traditionally, in the gridding algorithm (20), a very small kernel is used to reduce the computation. The errors associated with a small kernel are mitigated by oversampling the grid, and the associated image weighting is mitigated by a deapodization of the resulting image to correct the intensity weighting. The gridding algorithm in effect trades off complexity with tolerable accuracy errors. In the proposed reconstruction, the data acquisition consistency in Eq. 8 is enforced. Therefore, the consistent solution when using a nonsinc kernel cannot be exactly  $x_i$ , but a function of it,  $\tilde{x}_i$ . Let  $\tilde{c}$  be a convolution kernel such that  $c * \tilde{c} = \delta$ . Then

$$\tilde{x}_i = \tilde{c} * x_i, \quad [14]$$

so,  $c * \tilde{x}_i = c * \tilde{c} * x_i \approx x_i$ .

In the image domain, this function is manifested as a multiplication by a deapodizing function

$$\begin{aligned} \tilde{m}_i(r) &= \tilde{C}(r) m_i(r) \\ &= \frac{1}{C(r)} m_i(r), \end{aligned} \quad [15]$$

where  $m_i$ ,  $\tilde{m}_i$ ,  $\tilde{C}$ , and  $C$  denote the inverse Fourier transform of  $x_i$ ,  $\tilde{x}_i$ ,  $\tilde{c}$ , and  $c$ , respectively.

In the usual gridding reconstruction, such weighting is generally not a problem and is easily compensated. However, in our case, the solution  $\tilde{x}$  may no longer be consistent with the data calibration constraint in Eq. 6. This is in particular a problem when using a Kaiser-Bessel kernel, which has large variations across the imaged field of view. Any amplitude variation in the field of view will amplify residual aliasing. To mitigate this, one should design a kernel with ripple constraints on the passband, as well as the stop band. For example, a windowed-sinc kernel would introduce much less variation than the Kaiser-Bessel kernel would. An optimized alternative is to modify the min-max second order cone program (SOCP) interpolator by Beatty et al. (21) to include the image intensity variation constraint.

### Revisiting the Calibration

The grid oversampling in  $k$ -space requires that the calibration kernel support be increased by the same amount. For example, if normally one would choose to use a  $5 \times 5$  size kernel in a GRAPPA reconstruction and a grid oversampling is 1.2, then a  $6 \times 6$  size kernel should be used. In addition, the sampling trajectory of the calibration region must be oversampled to support the larger. Field of view of the oversampled grid or else the fidelity and integrity of the calibration may be compromised. Finally, the interpolation kernel that grids the calibration region should have as little passband ripple as possible, again to ensure the fidelity of the calibration process.

### Reconstruction

The steps for non-Cartesian  $k$ -space-based reconstruction are as follows:

- Design an appropriate interpolation kernel based on a specific maximum aliasing amplitude, image weighting, kernel width, and grid oversampling
- Perform a calibration that supports the oversampled grid size to obtain the calibration weights
- Solve Eq. 10 using the CG algorithm to obtain reconstructed Cartesian  $k$ -space data for all coils
- Reconstruct the images by computing the inverse Fourier transform
- Crop to the desired grid size
- Apodize the images by multiplying with the inverse Fourier transform of the interpolation kernel.

It is important to note that an efficient and numerically stable implementation of the POCS approach for non-Cartesian imaging is challenging for reasons outside the scope of this paper; therefore, we prefer the (CG) approach in this case. A diagram for the CG algorithm implementation is described in detail in Fig. 2a. The top part calculates the gradient of the objective function as described by Eq. 11. The current estimate of  $k$ -space (on the oversampled grid) is split into two paths. The left path computes the gradient of

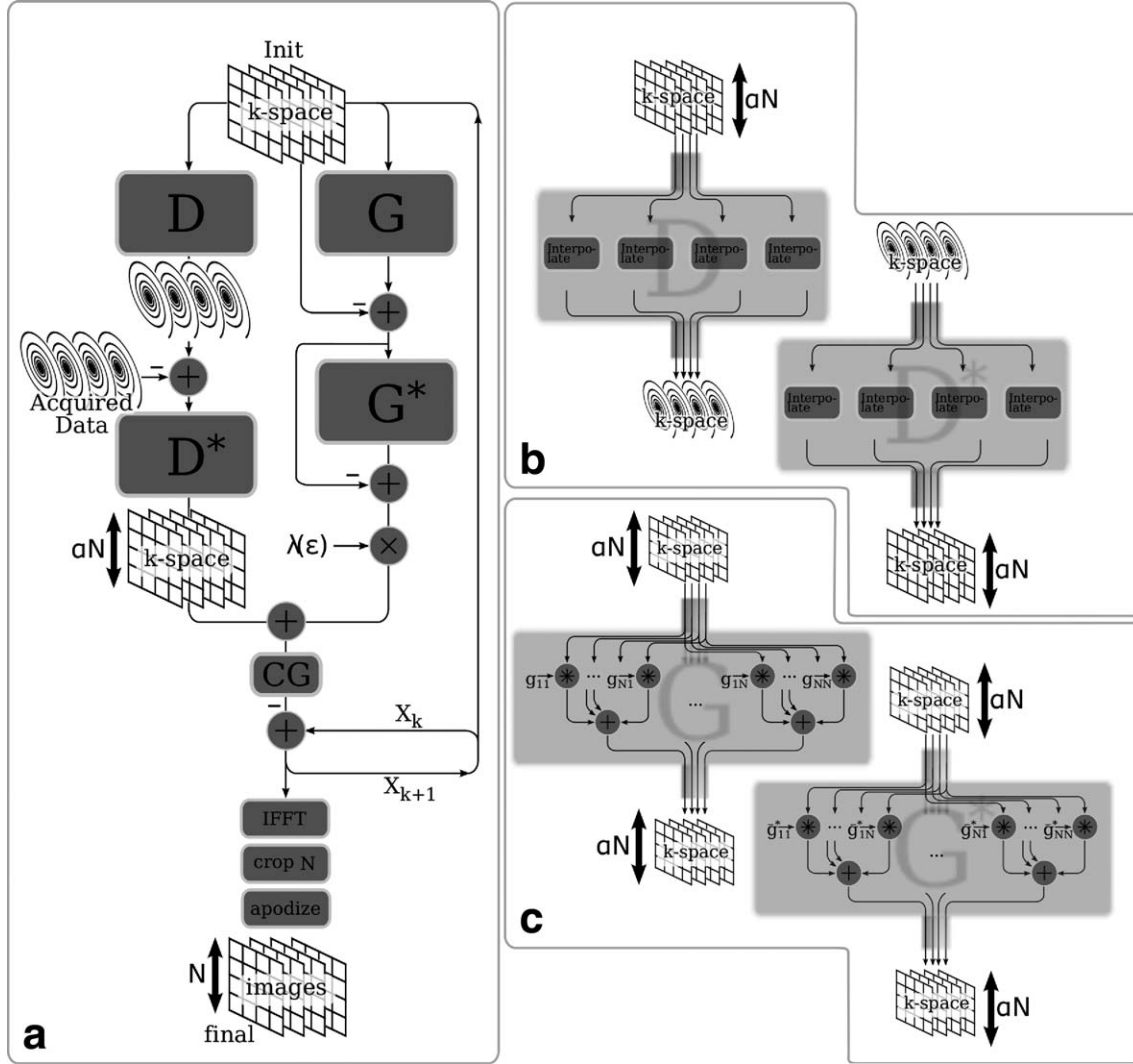


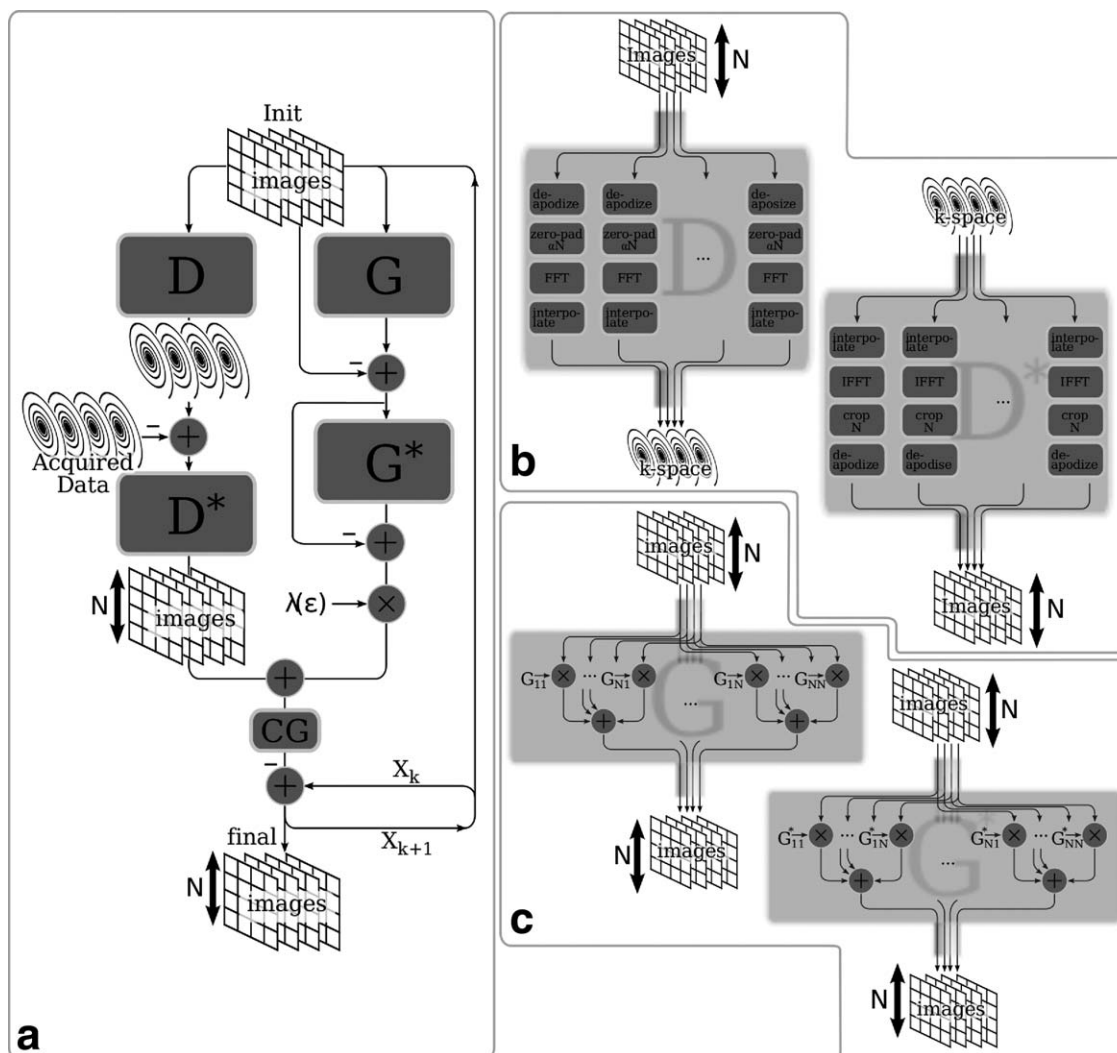
FIG. 2. *k*-Space-based reconstruction. **a**: Illustration of the CG algorithm for non-Cartesian consistency constrained reconstruction in *k*-space. **b**: Illustration of the interpolation operator,  $D$ , and its adjoint,  $D^*$ . **c**: Illustration of the calibration consistency operator,  $G$ , and its adjoint,  $G^*$ . The notation  $\hat{g}_{ji}^*$  stands for an inverted conjugated version of the filter  $g_{ji}$ .

the acquisition data consistency term by interpolating the current estimate onto a non-Cartesian grid and then computing the difference error with the acquired data and interpolating that error back onto a Cartesian grid. The right path computes the gradient of the calibration data consistency by performing the SPIRiT convolution, convolving the result with its adjoint, and finally scaling with  $\lambda$ . The calculated gradient is then used to find a CG direction, which is subtracted from the previous estimate of *k*-space. After the iterations converge, an inverse fast Fourier transform (FFT) is performed for each coil and the images are cropped to the appropriate field of view and apodized by the inverse Fourier transform of the *k*-space convolution interpolation kernel.

Figures 2b and c detail the computation of the  $G$  and  $D$  operators and their adjoints. The  $D$  operator is simply a convolution interpolation from an oversampled Cartesian grid onto a non-Cartesian grid. Its adjoint turns out to be a convolution interpolation from a non-Cartesian grid to an

oversampled Cartesian grid. The  $G$  operator performs the *k*-space convolutions with the calibrated SPIRiT kernels. Its adjoint performs similar convolutions but the SPIRiT kernels are reordered, flipped (in both the horizontal and vertical axis), and conjugated.

The *k*-space implementation has the advantage of not requiring a Fourier transform during the iterations. However, it has some disadvantages. To comply with the bandpass ripple requirement, the interpolation kernel is inevitably larger than what is commonly used for gridding (for the same interpolation error and grid oversampling). In addition, the calibration consistency convolution has to be performed on an oversampled grid size, with a larger calibration kernel. These increase the complexity of the operations in each iteration of the reconstruction. At some point, depending on the size of the interpolation kernel and calibration kernel, the grid size, and the specific machine that is used for reconstruction, the operations in *k*-space may be more costly than performing similar operations in



The advantage here is that large calibration kernels do not incur further increase in computational complexity since the convolution is implemented as a multiplication in image space. Figure 3 illustrates the CG reconstruction



of Eq. 16 and the implementation of the  $D$  and  $G$  operators. The algorithm flow is similar to the  $k$ -space implementation, except for a few details. The  $D$  and  $D^*$  operators perform the inverse-gridding and gridding algorithms and the  $G$  and  $G^*$  operators perform image multiplications instead of convolutions. Another difference is that after the CG iterations converge, the result is the reconstructed images and no further processing is required.

### Off-Resonance Correction

One of the advantages of representing the reconstruction as a solution to a system of linear equations is that it is possible to easily incorporate off-resonance variation in the reconstruction. This is particularly important for non-Cartesian trajectories, where off-resonance frequencies lead to image blurring. The off-resonance correction appears in the data consistency constraint in Eq. 16 by modifying the nuFFT operator  $D$  to include off-resonance information. Denote  $\phi_n(r)$  to be a complex vector with unit magnitude elements. The phase of  $\phi_n(r)$  represents the phase of the image, contributed by off-resonance at the time the sample  $k(n)$  is acquired. The part of the operator  $D$  that operates on the  $i$ th coil image is,

$$y_i(n) = \int \delta(k(n) - r) \left\{ c * \text{FFT}_{\text{aN}} \left( \frac{m_i \phi_n}{C} \right) \right\} (r) dr. \quad [19]$$

Efficient ways to implement this operator are to approximate it using multifrequency and time-segmented reconstruction approaches, as described elsewhere (23,24).

**Regularization.** Since Eq. 10 is described as an optimization, one can include additional terms in the objective function, as well as constraints that express prior knowledge in the reconstruction. Consider the optimization problem

$$\underset{x}{\text{argmin}} \quad \|Dx - y\|^2 + \lambda_1 \|(G - I)x\|^2 + \lambda_2 R(x) \quad [20]$$

where the function  $R(x)$  is a penalty function that incorporates the prior knowledge. This formulation is very flexible because the penalty can be applied on the image, as well as  $k$ -space data. Denoting  $W$  as a data weighting function,  $\nabla\{\}$  as a finite-difference operator, and  $\Psi\{\}$  as a wavelet operator, here are some examples of potential penalties:

$$R(x) = \|x\|_2, \quad \text{Tikhonov regularization}$$

$$R(x) = \|Wx\|_2, \quad \text{Weighted Tikhonov regularization}$$

$$R(x) = \|\nabla\{\text{IFFT}(x)\}\|_1, \quad \text{Total variation}$$

$$R(x) = \|\Psi\{\text{IFFT}(x)\}\|_1, \quad \ell_1 \text{ wavelet.}$$

The last two are  $\ell_1$  penalties and are increasingly popular due to the theory of compressed sensing (25).

## RESULTS

All the reconstructions were implemented in MatLab (The MathWorks, Inc., Natick, MA). The image-based non-Cartesian reconstruction used Fessler and Sutton's (22) NUFFT code. The  $\ell_1$  wavelet regularized reconstruction used Buchheit and Donoho's (26) Wavlab code. The CG

algorithm used was LSQR (27). In the spirit of reproducible research (28), we provide a software package to reproduce some of the results described in this paper. The software can be downloaded from <http://www.eecs.berkeley.edu/~mlustig/software/>.

### Noise and Artifacts Measurements

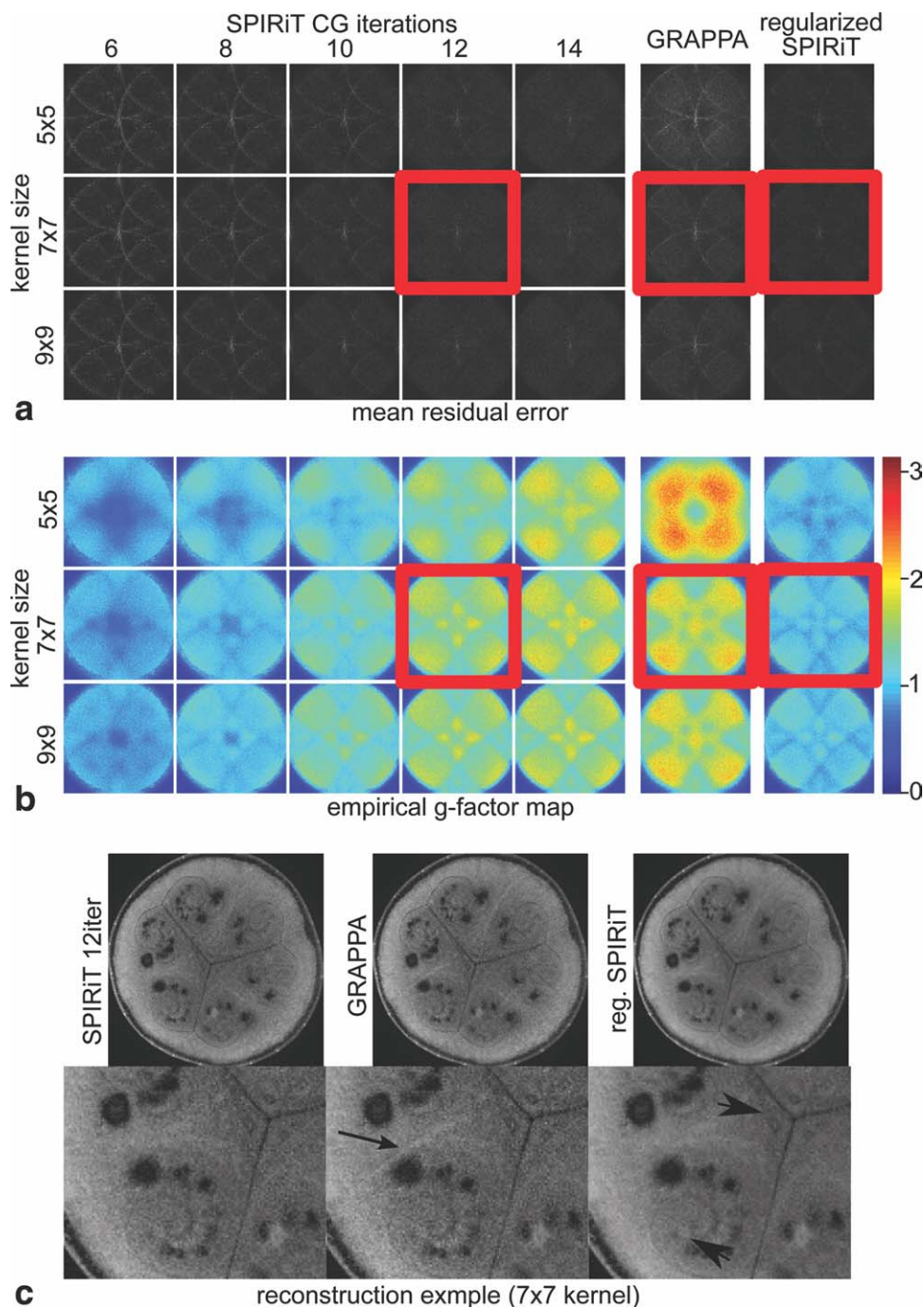
To evaluate the noise and reconstruction properties of SPIRiT in comparison to the original GRAPPA method, we constructed the following experiment: We repeatedly scanned an axial 2D slice of a watermelon 100 times, using a balanced steady state free-precession sequence with scan parameters echo time = 2.5 ms, pulse repetition time = 6.4 ms, flip = 60°, bandwidth (BW) = 62.5 kHz. The slice thickness was 5 mm, field of view of 16.5 × 16.5 cm, and a matrix size of 256 × 256, corresponding to 0.65 × 0.65 mm in-plane resolution. The scan was performed on a GE Signa-Excite 1.5-T scanner (GE, Waukesha, WI), using an eight-channel receive-only head coil. To compensate for temporal phase drift between scans, a 4th order complex polynomial was fitted and removed from each pixel time course. To compensate for the readout filter roll-off, the images were cropped to 246 × 246 pixels, from which 100 2D  $k$ -space data sets were synthesized by computing a Fourier transform for each (complex valued) image. Each  $k$ -space data set was then undersampled uniformly by a factor of 4 (2 × 2 in each dimension) while keeping a fully sampled 24 × 24 area for calibration.

The data were processed in the following way: Each data set was reconstructed several times, using traditional GRAPPA, each time with a different kernel size (5 × 5, 7 × 7, and 9 × 9). The GRAPPA kernels were calibrated for each unique local sampling pattern set. In addition, each data set was reconstructed using the  $k$ -space-based Cartesian SPIRiT, with equality data consistency of Eq. 12, again with 5 × 5, 7 × 7, and 9 × 9 kernel sizes. The SPIRiT reconstruction was implemented using the LSQR (27) CG algorithm. To show the dependency of the reconstruction on the number of iterations, the results at the 6th, 8th, 10th, 12th, and 14th were saved. Finally, each data set was reconstructed with SPIRiT with  $\ell_1$ -norm wavelet regularization. The wavelet regularization parameter was empirically set to 0.015. For each of the above experiments, the resulting reconstructed coil images were combined with square root of sum of squares. Following the reconstructions, the mean difference error with the fully sampled data set was calculated. In addition, the standard deviation for each pixel across the 100 scans was computed and normalized by the standard deviation of the pixels in the full set (taking into account the reduced scan time) to obtain empirical noise amplification ( $g$ -factor maps) estimates.

Figure 4a-c shows the results of the experiments. Figure 4a left columns show the residual error in the SPIRiT reconstruction as a function of kernel size and number of CG iterations. Overall, the reconstruction is insensitive to the kernel size, achieving similarly low residual in all cases (after a sufficient number of iterations), with slightly more accurate results for the larger kernel sizes. The iterations seem to converge slightly faster for larger kernel sizes as well. The sixth column shows the residual GRAPPA reconstructions for the different kernel sizes. The reconstruction



FIG. 4. Empirical reconstruction error and noise amplification maps of SPIRiT, GRAPPA, and  $\ell_1$ -wavelet regularized SPIRiT obtained from 100 scans, using eight channels and 4-fold acceleration. **a**: The mean residual of SPIRiT as a function of kernel size and number of CG iterations show convergence around 10-12 iterations and overall insensitivity to kernel size. GRAPPA exhibits larger residuals than SPIRiT, especially for smaller kernel sizes. The  $\ell_1$ -wavelet regularization does not reduce the accuracy of the reconstruction (e.g., does not introduce image blurring). **b**: The empirical  $g$ -factor maps demonstrate the inherent regularization and noise reduction in early termination of CG. SPIRiT exhibits an overall lower noise amplification than GRAPPA for similar residual error. The  $\ell_1$ -wavelet regularization exhibits almost no noise amplification at all. **c**: Reconstruction example. The black arrow points to residual aliasing in GRAPPA that is absent in SPIRiT. The arrowheads point to significant noise reduction in the  $\ell_1$ -wavelet regularized SPIRiT.



shows reduction in the residual with larger kernel size; however, the residual is significantly larger than all the SPIRiT reconstructions. The seventh column shows the  $\ell_1$ -wavelet regularized SPIRiT residual for all the kernel sizes. They exhibit slightly lower residual, similar to the nonregularized SPIRiT, which means that the regularization does not harm the accuracy of the reconstruction.

Figure 4b shows the empirical  $g$ -factor maps. Figure 4b left columns show the noise maps in the SPIRiT as a function of kernel size and number of CG iterations. It shows that as the solution becomes more accurate, the noise in the reconstruction is increased. At some point (10-12 iterations), it is worthwhile to terminate the

reconstruction as the CG iterations start fitting the noise. The figure also shows that the noise amplification in SPIRiT is lower than in GRAPPA. This is because the algorithm uses the data more efficiently and also because of the early termination of the CG iterations. The seventh column shows that the  $\ell_1$ -wavelet regularized SPIRiT has almost no noise amplification, with  $g$ -factor less than or equal to 1 in most locations. This reconstruction offers the advantage of eliminating the  $g$ -factor without trading off reconstruction accuracy or resolution.

Figure 4c shows a reconstruction example corresponding to the residual error and empirical  $g$ -factor maps that are marked by red boxes. The black arrow shows some residual

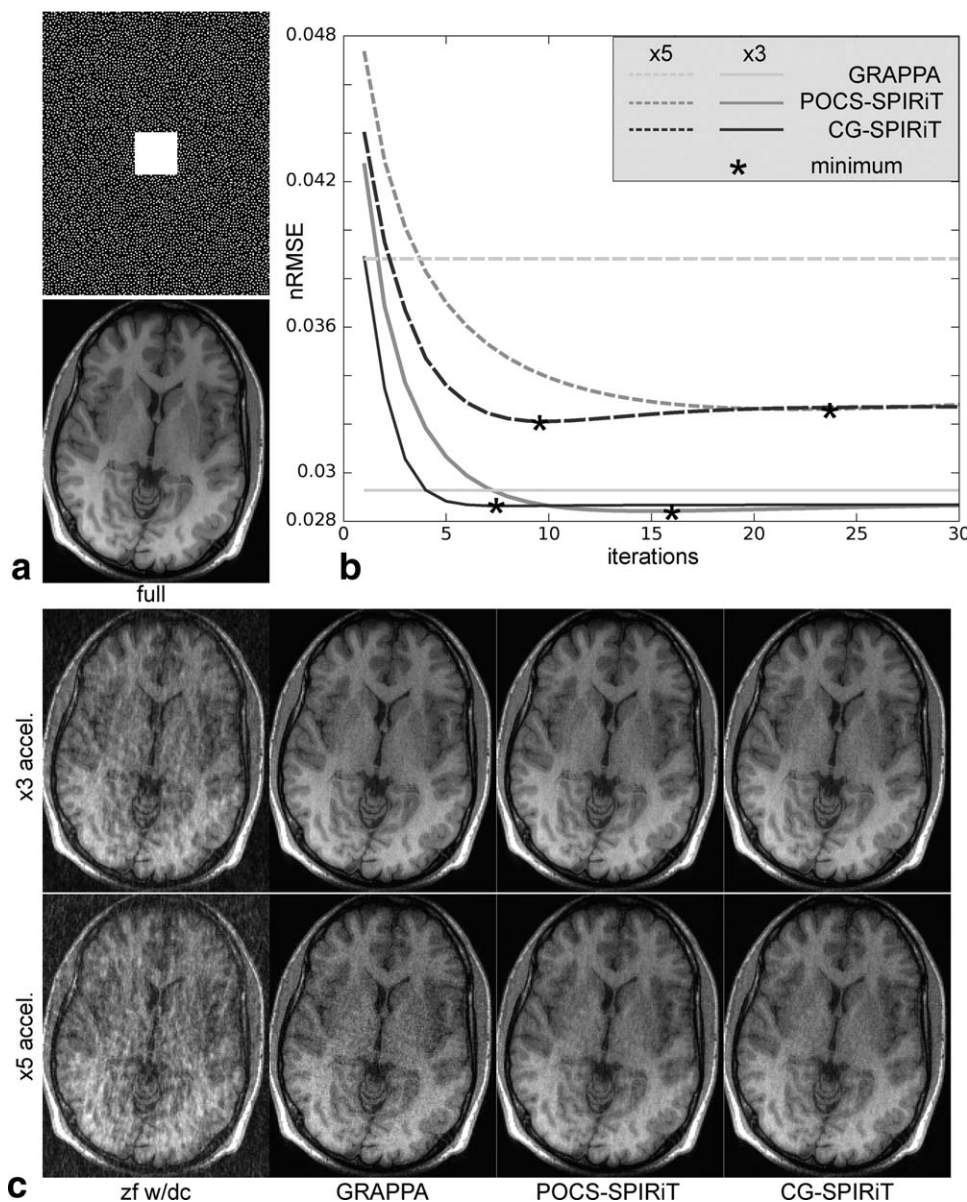


FIG. 5. CG-SPIRiT and POCS-SPIRiT from 3-fold and 5-fold arbitrary Cartesian sampling using eight channels. **a**: five-fold acceleration Poisson-Disc density sampling pattern and the reconstruction from the full data. **b**: Normalized RMSE (nRMSE) as a function of iterations. The advantage of SPIRiT shows at higher acceleration where efficient use of the acquired data becomes crucial. **c**: Examples of the various reconstruction. Note the reduction in noise and artifacts in the SPIRiT reconstructions from 5-fold accelerated data.

aliasing in the GRAPPA reconstruction that is absent from both the SPIRiT reconstructions. The arrowheads point out significant noise reduction without loss of detail in the  $\ell_1$ -wavelet regularized SPIRiT.

#### Arbitrary Cartesian Sampling

The SPIRiT reconstruction can easily cope with arbitrary sampling patterns. In addition, it makes efficient use of all the acquired data in the reconstruction. This becomes important at higher accelerations where signal-to-noise ratio efficiency and good artifact reduction become key ingredients for success. To demonstrate these qualities, we performed the following experiments. A  $T_1$ -weighted, inversion recovery prepared, 3D, spoiled gradient echo (SPGR) sequence was used to obtain a fully sampled high-resolution data set of a brain of a healthy volunteer. The scan parameters were echo time = 8 ms, pulse repetition

time = 17.6 ms, flip =  $20^\circ$ ,  $BW$  = 6.94 kHz. The field of view was  $20 \times 20 \times 20$  cm, with a matrix size of  $200 \times 200 \times 200$ , corresponding to isotropic  $1 \text{ mm}^3$  resolution. The scan was performed on a GE Signa-Excite 1.5-T scanner, using an eight-channel receive coil.

A single slice of this data set was chosen for the experiment. Two undersampling patterns were designed by choosing samples according to a Poisson-Disc sampling density (29). One data set was undersampled by a factor of 3 and the second by a factor of 5. A fully sampled area of  $30 \times 30$  samples was left in the center of  $k$ -space for calibration. An example of the 5-fold accelerated sampling pattern is shown in Fig. 5b. The undersampled data sets were reconstructed using Cartesian GRAPPA, POCS Cartesian SPIRiT, and CG Cartesian SPIRiT, followed by a square root of sum-of-squares combination of the coil images. Following the reconstruction, the normalized root mean squared error with the fully sampled reference was

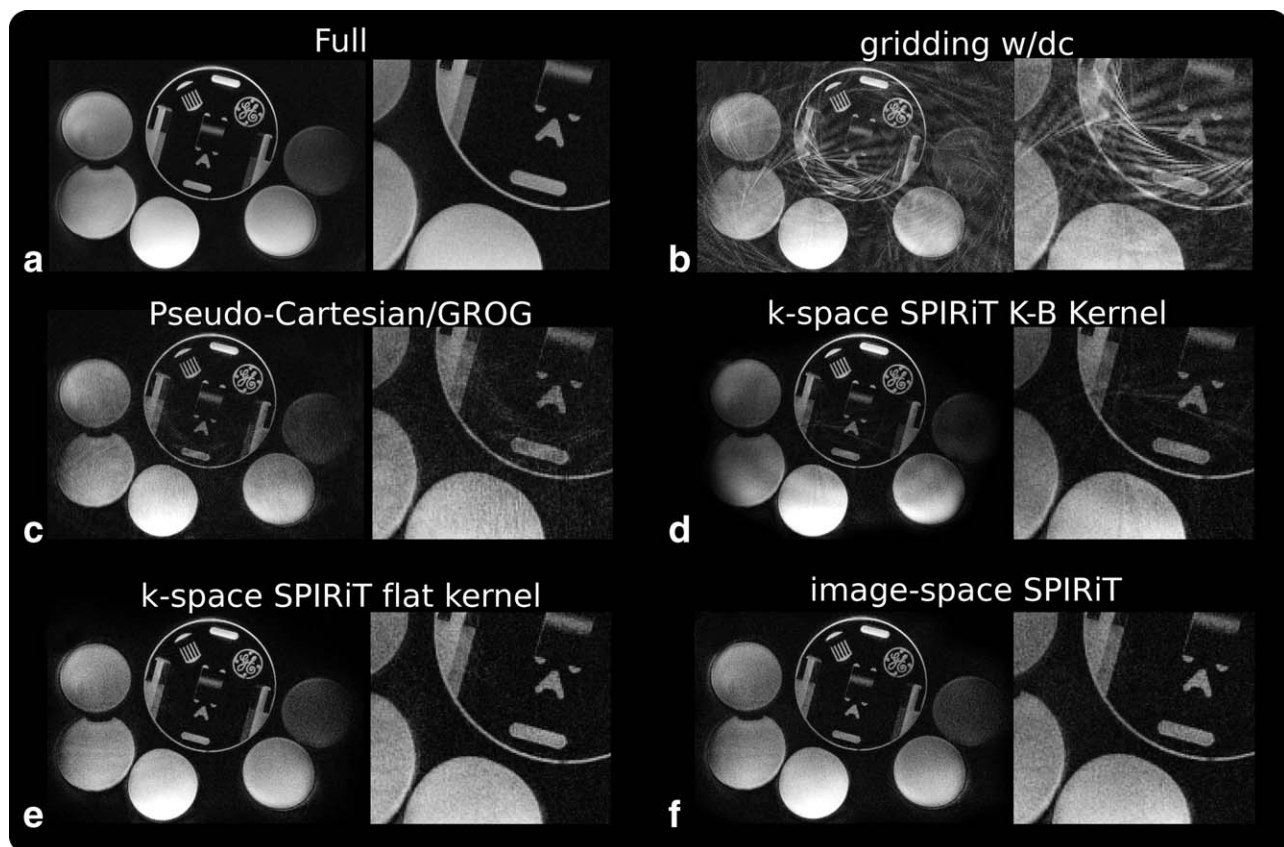


FIG. 6. Non-Cartesian SPIRiT reconstruction from 3-fold undersampled spirals and four channels. **a**: Reconstruction from fully sampled data. **b**: Gridding with density compensation. **c**: Pseudo-Cartesian GRAPPA with GROG. **d**:  $k$ -Space SPIRiT with Kaiser-Bessel interpolator kernel. **e**:  $k$ -Space SPIRiT with flat passband interpolator kernel. **f**: Image-space SPIRiT.

calculated using the formula normalized root mean square error (nRMSE) =  $\frac{1}{\max(x) - \min(x)} \sqrt{\frac{1}{N} \sum_{i=0}^{N-1} (x(i) - \bar{x}(i))^2}$ . The SPIRiT and the GRAPPA reconstructions used a  $7 \times 7$  size kernel.

Figure 5a shows the reconstruction from the full data, as well as the 5-fold accelerated sampling pattern. Figure 5b shows plots of the nRMSE of the reconstructions as a function of iterations. The solid and dashed lines correspond to the 3-fold and 5-fold accelerated acquisitions, respectively. The minimum nRMSE is marked by asterisk. Figure 5c shows example of the reconstructions. At 3-fold acceleration, all reconstructions perform similarly well and are capable of reconstructing good-quality images from the undersampled data. The SPIRiT reconstructions have only slightly lower nRMSE than GRAPPA. This is because at 3-fold acceleration with eight channels, the reconstruction is well conditioned. At higher acceleration, where each data measurement counts, the difference in the reconstruction becomes more significant. The SPIRiT reconstructions at 5-fold acceleration have about 18% better nRMSE than the GRAPPA reconstruction. The difference in noise amplification and artifact suppression becomes much more apparent in the reconstructed images. Other details that are worth mentioning are that CG-SPIRiT converges faster than POCS, with eight iterations for CG and 16 iterations for POCS at 3-fold acceleration and with 10 iterations for CG and 24 iterations for POCS at 5-fold acceleration. However each

POCS iteration is computationally cheaper than each CG iteration. The regularization property of early termination of CG is also apparent in Fig. 5b, where after some iterations the error starts increasing as noise is being fitted. It is important to note that the nRMSE is not always a decreasing function because it is the normalized energy of the difference between the reconstruction and the original acquired data (which is normally not given). It should not be confused with the residual of the objective function, which is nonincreasing.

#### Phantom Non-Cartesian Reconstruction

To demonstrate non-Cartesian SPIRiT reconstruction, we scanned a phantom, using a spiral gradient echo sequence. The phantom chosen contains sharp edges and many image voids, which make it particularly difficult to estimate sensitivity maps and therefore is ideal for an autocalibrating reconstruction. The spiral trajectory was designed with 60 interleaves, 30-cm field of view, and 0.75 mm in-plane resolution. The readout time was kept short, only 5 ms, to avoid off-resonance effects. The scan was performed on a GE Signa-Excite 1.5-T scanner, using a four-channel cardiac coil. A reconstruction from the full data set is shown in Fig. 6a.

First, a Cartesian calibration area ( $32 \times 32$ ) was reconstructed from the full data set. These Cartesian  $k$ -space data were used to calibrate the SPIRiT kernel and also the

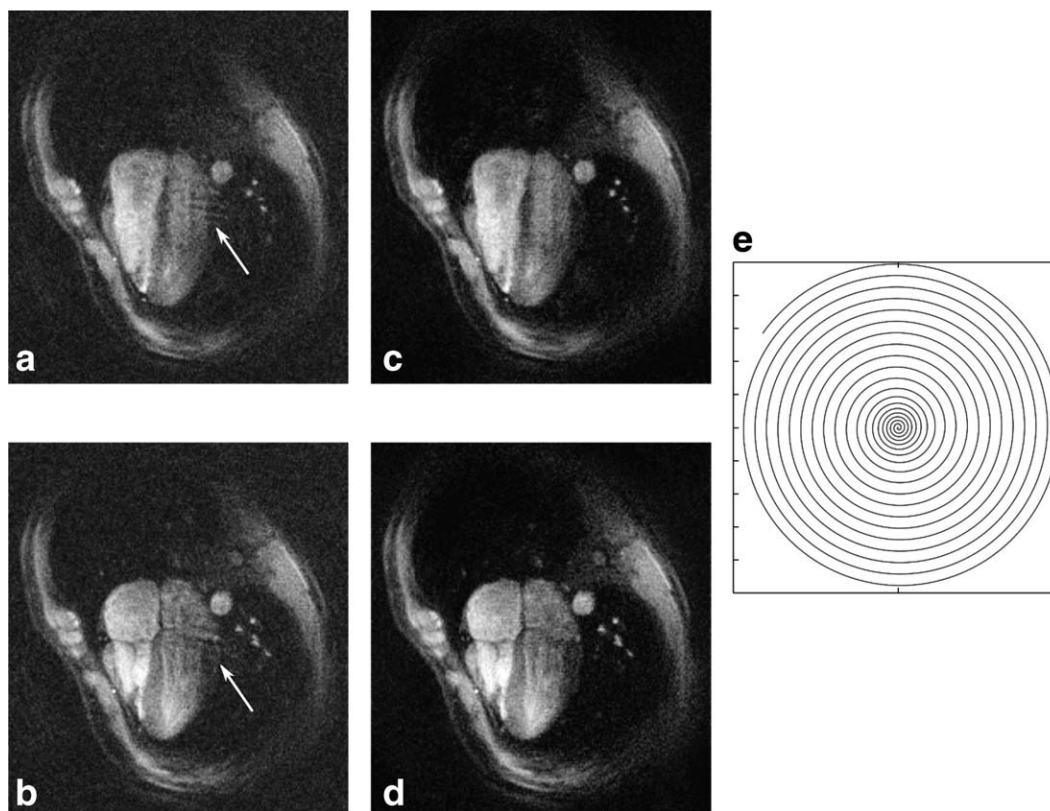


FIG. 7. Dynamic cardiac imaging with dual-density spirals with 3-fold acceleration and four channels. Two phases of a four-chamber view of the heart. **a,b**: Sum of squares of gridding reconstruction exhibits coherent (arrows) and incoherent (noiselike) aliasing artifacts. **c,d**: Both the coherent and incoherent artifacts are removed by SPIRiT. **e**: One out of the three spiral interleaves.

GRAPPA operator gridding (GROG) and pseudo-Cartesian GRAPPA (16) kernels. Then, the data set was under-sampled by a factor of 3 by choosing 20 out of the 60 interleaves.

In this experiment, we performed several different reconstructions. Our aim was to evaluate the quality of the image-domain and  $k$ -space-domain SPIRiT methods, to demonstrate the importance of using a flat passband kernel for the  $k$ -space SPIRiT, and to compare to existing reconstructions. We performed five reconstructions corresponding to Fig. 6b-f: Fig. 6(b). The standard gridding reconstruction with density compensation shows, as expected, significant aliasing artifacts. A pseudo-Cartesian/GROG reconstruction was provided for us courtesy of Dr. Nicole Seiberlich (Fig. 6c). It used GROG to grid the data and then pseudo-Cartesian GRAPPA with six source points for each pattern, with an overall number of 249 patterns. The reconstruction is able to reduce the artifacts; however, aliasing artifacts are still visually apparent and noise is increased. This is because this method performs parallel imaging twice, once in the gridding stage and once in the unaliasing stage. Since the number of coils is relatively small, artifacts in one are propagated and amplified in the other. The  $k$ -space SPIRiT with Kaiser-Bessel kernel parameters were Kaiser-Bessel kernel width = 7pixels, 1.25 grid oversampling,  $7 \times 7$  SPIRiT kernel size, 15 CG iterations (Fig. 6d). The reconstruction exhibits some residual artifacts due to the inconsistency introduced by the image weighting of the Kaiser-Bessel interpolator. The flat passband kernel

was designed by modifying the numerical optimization by Beatty et al. (21) (Fig. 6e). The design criteria were width = seven pixels, 0.25 passband ripple, 0.005 stop-band ripple, and 1.25 grid oversampling. In addition, a  $7 \times 7$  SPIRiT kernel size was used and 15 CG iterations were performed. The reconstruction exhibits significant reduction of artifacts compared to the previous reconstruction. The image-based SPIRiT used Fessler's min-max NUFFT with  $\times 2$  grid oversampling (Fig. 6f). A  $7 \times 7$  SPIRiT kernel, implemented as image multiplications, was used and 15 CG iterations were performed. The reconstruction exhibits slightly better artifact suppression than the  $k$ -space method. In the MatLab implementation, the reconstruction time of the  $k$ -space and image-space methods was similar. The value for  $\lambda$  in the non-Cartesian SPIRiT reconstructions was chosen using an L-curve analysis to be  $\lambda = 1$ .

#### In Vivo Non-Cartesian Reconstruction

To demonstrate the image-based non-Cartesian reconstruction in-vivo, we performed a dynamic heart study, using a three-interleaf dual-density, spiral, gradient-echo sequence. The spiral trajectory was designed to support a field of view ranging from 35 cm in the center to 10 cm (3-fold acceleration) in the periphery. The in-plane resolution was 1.5 mm, with readout time of 16 ms; slice thickness was 5 mm. The pulse repetition time was set to 25 ms achieving a sliding-window temporal resolution of 40 frames per second (FPS). The trajectory is illustrated in Fig. 7e. The scan



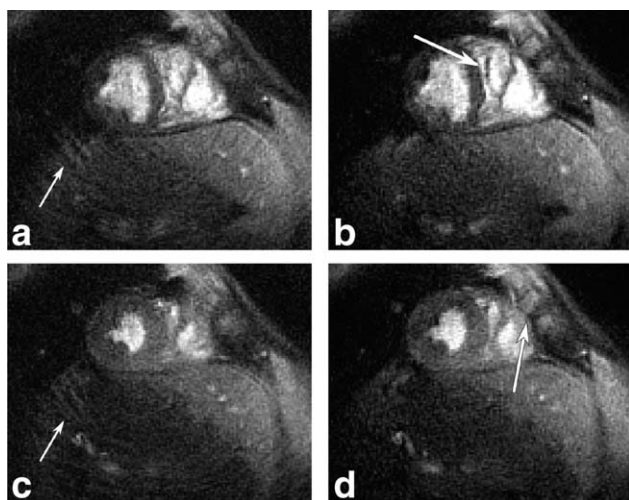


FIG. 8. Dynamic cardiac imaging with dual-density spirals and off-resonance correction with 3-fold acceleration and four channels. Two phases of a short-axis view of the heart. **a,b**: Sum of squares of gridding reconstruction exhibits coherent (arrows), incoherent (noiselike) aliasing artifacts and blurring due to off-resonance. **c,d**: SPIRiT reduces both the coherent and incoherent artifacts, as well as deblurring the image (arrows).

was performed using the rtHawk real-time MRI system (30), installed on a GE Signa-Excite 1.5-T scanner with a four-channel cardiac coil. The data for each sliding window image were reconstructed using the image-based SPIRiT algorithm. To speed up the reconstruction, the previous image was used as an initial image for the reconstruction of the next image frame. This way, seven CG iterations were sufficient for good image quality.

Figure 7 shows two frames in the cardiac cycle. The gridding reconstruction images (Fig. 7a and b) suffer from coherent (arrows) and incoherent artifacts due to the under-sampling. These artifacts are removed by SPIRiT.

#### Off-Resonance Correction

To demonstrate the iterative multifrequency off-resonance correction capabilities of the reconstruction, we applied the same scan parameters as in the previous section to a short-axis dynamic view of the heart. Prior to the acquisition, a field map measurement was taken. As a data consistency operator, we used the approach described by Sutton et al. (24).

Figure 8 shows the result of off-resonance corrected SPIRiT compared to a gridding reconstruction with no off-resonance correction. SPIRiT is able to suppress the coherent and incoherent aliasing, as well as deblurring the image.

#### $\ell_1$ -Norm Wavelet Regularization

To demonstrate the regularization capabilities of SPIRiT, we performed a postcontrast three-dimensional spoiled gradient echo scan, using a 12-channel body coil. The pulse repetition time was 3.3 ms, with a flip angle of  $15^\circ$ . The Field of view was set to 35 cm, with an image matrix of  $192 \times 192 \times 88$  readout, phase encodes and slice encodes, respectively. Images were reconstructed using standard 2D GRAPPA parallel imaging reconstruction. Images were also reconstructed using SPIRiT with  $\ell_1$  wavelet (Daubechies 4) regularization.

Figure 9 illustrates the result of the reconstructions. It shows that the nonregularized 2D GRAPPA reconstruction

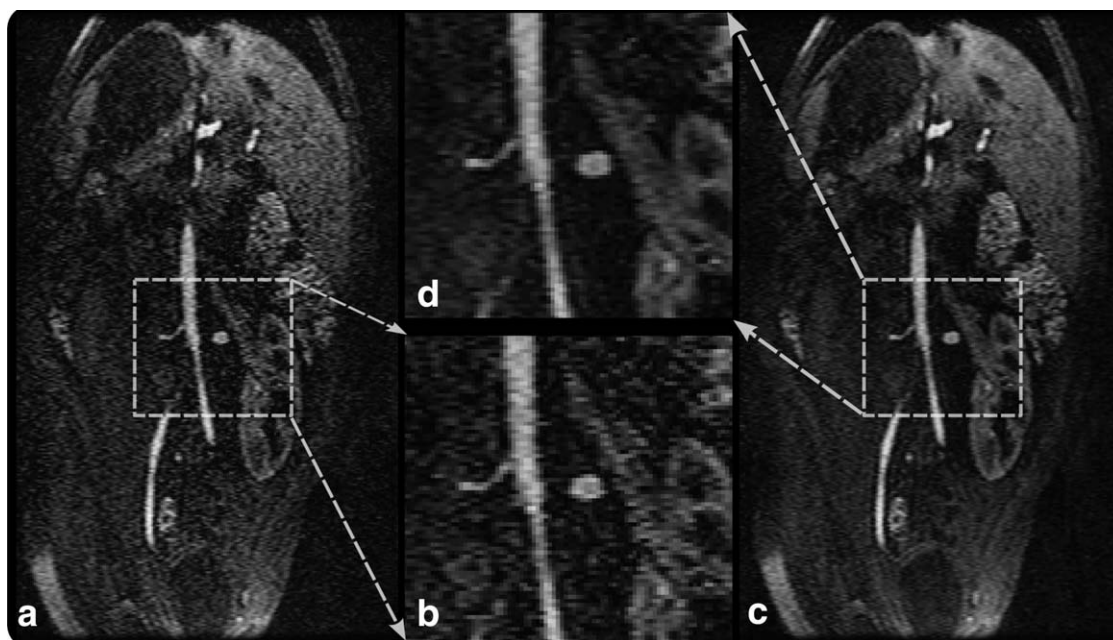


FIG. 9.  $\ell_1$ -wavelet regularization of 4-fold accelerated postcontrast abdomen scan with a 12-channel body coil. **a**: the nonregularized GRAPPA reconstruction exhibits noise amplification due to the  $g$  factor, especially in the middle of the image. **b**: Zoomed-in GRAPPA reconstruction. **c**: The noise amplification is suppressed in the  $\ell_1$ -wavelet regularized SPIRiT reconstruction, while the edges and features in the image are preserved. **d**: Zoomed-in  $\ell_1$ -wavelet regularized SPIRiT reconstruction.

exhibits increased noise, especially in the center of the image, due to the  $g$  factor. This noise is suppressed by the  $\ell_1$  regularized SPIRiT reconstruction, while the edges and features in the image are preserved.

## DISCUSSION

There are several possible extensions to SPIRiT. The SPIRiT reconstruction offers better noise performance than GRAPPA. However, optimization of the kernel for even better noise performance is possible. For example, one can use a scheme similar to that of Samsonov (31) to optimize the kernel calibration. In addition to optimizing the kernel for noise, one can optimize noise performance by including noise covariance matrices in the SPIRiT reconstruction, as described in Pruessmann et al. (4).

As an iterative reconstruction, the computational complexity of SPIRiT can be more intensive than direct reconstruction, especially for simple cases such as uniform undersampling. The Cartesian POCS algorithm requires in each iteration an operation similar to a single GRAPPA reconstruction. The algorithm often requires somewhere between 10 and 40 iterations to converge. The CG Cartesian algorithm requires two GRAPPA-type operations per iteration. However, it is more flexible, is more stable, and often converges faster (six to 20 iterations) than the POCS algorithm. In general, we tend to prefer the CG approach over POCS; however, the simplicity of POCS is attractive conceptually and also in implementation. The CG non-Cartesian algorithm requires two GRAPPA-type operations and two gridding operations (for each coil) per iteration.

The SPIRiT approach has an advantage in reconstructions from highly nonuniform sampling patterns. In traditional GRAPPA reconstruction from such sampling schemes, there is a need to perform calibration for numerous sampling patterns. For example, in the Poisson-Disc sampling pattern presented earlier, there were approximately 25,000 individual patterns. The calibration stage for SPIRiT is negligible because SPIRiT uses only a single pattern. In such cases, the difference in reconstruction times may be significantly reduced.

Although our results comparing the  $k$ -space domain and image-domain non-Cartesian SPIRiT are not conclusive, we tend to prefer the image-domain approach and find it easier to use for several reasons: The choice of parameters in the image-domain approach is straightforward, the gridding algorithm is unchanged, and the choice of the SPIRiT kernel size is the same as Cartesian SPIRiT and is independent of the the gridding parameters. On the other hand, in the  $k$ -space approach, the gridding has an additional passband ripple parameter in the kernel design, and the tradeoffs are less obvious because the choice of grid oversampling affects the SPIRiT kernel size. In addition to all the above, if image-based regularization is used (and it should be used!), then the image-domain approach is natural and much more efficient.

In all our experiments, the SPIRiT reconstruction had better noise performance than other GRAPPA-like algorithms, especially when the acceleration is pushed to the limit. This is mostly because SPIRiT uses the acquired data more efficiently. SPIRiT uses a small local kernel in  $k$ -space. However, because of the the SPIRiT operation is

repeated in every iterations, the “information” propagates in  $k$ -space and acquired data in one location of  $k$ -space affect the reconstruction of  $k$ -space locations far beyond the kernel radius. This has an averaging effect of noise, and the overall noise is reduced.

## CONCLUSIONS

We have presented SPIRiT, a self-consistency formulation for coil-by-coil parallel imaging reconstruction. The reconstruction can be solved efficiently, using iterative methods for data acquired on arbitrary  $k$ -space trajectories. We presented two variants of the reconstruction; image domain and  $k$ -space domain. In the  $k$ -space domain reconstruction, we introduced new requirements for  $k$ -space interpolation. In addition, we demonstrated that the formulation is easily extendible to include other techniques such as regularization and off-resonance correction. We showed that enforcing consistency constraints results in better conditioning, more accurate reconstruction, and better noise behavior than the traditional GRAPPA-like approaches.

## ACKNOWLEDGEMENTS

The authors thank Nicole Seiberlich for her help with the pseudo-Cartesian GRAPPA reconstruction. This work was supported by GE Healthcare.

## REFERENCES

1. Roemer PB, Edelstein WA, Hayes CE, Souza SP, Mueller OM. The NMR phased array. *Magn Reson Med* 1990;16:192–225.
2. Kelton JR, Magin RL, Wright SM. An algorithm for rapid image acquisition using multiple receiver coils. In: *Works in Progress, Eighth Annual Meeting and Exhibition of the SMRM*. Amsterdam: Society of Magnetic Resonance in Medicine, 1989. p 1172.
3. Sodickson DK, Manning WJ. Simultaneous acquisition of spatial harmonics (SMASH): fast imaging with radiofrequency coil arrays. *Magn Reson Med* 1997; 38:591–603.
4. Pruessmann KP, Weiger M, Scheidegger MB, Boesiger P. SENSE: sensitivity encoding for fast MRI. *Magn Reson Med* 1999;42:952–962.
5. Pruessmann KP, Weiger M, Börner P, Boesiger P. Advances in sensitivity encoding with arbitrary  $k$ -space trajectories. *Magn Reson Med* 2001;46:638–651.
6. Kyriakos W, Panych L, Kacher D, Westin C, Bao S, Mulkern R, Jolesz F. Sensitivity profiles from an array of coils for encoding and reconstruction in parallel (SPACE RIP). *Magn Reson Med* 2000;44:301–308.
7. Yeh E, McKenzie C, Ohliger M, Sodickson D. Parallel magnetic resonance imaging with adaptive radius in  $k$ -space (PARS): constrained image reconstruction using  $k$ -space locality in radiofrequency coil encoded data. *Magn Reson Med* 2005;53:1383–1392.
8. Liu C, Bammer R, Moseley M. Parallel imaging reconstruction for arbitrary trajectories using  $k$ -space sparse matrices (kSPA). *Magn Reson Med* 2007;58:1171–1181.
9. Blaimer M, Breuer F, Mueller M, Heidemann R, Griswold MA, Jacob P. SMASH, SENSE, PILS, GRAPPA: how to choose the optimal method. *Top Magn Reson Imaging* 2004;15:223–236.
10. Jakob P, Griswold MA, Edelman R, Sodickson D. AUTO-SMASH: a self-calibrating technique for SMASH imaging. *Simultaneous Acquisition of Spatial Harmonics*. *MAGMA* 1998;7:42–54.
11. Heidemann R, Griswold MA, Haase A, Jakob P. VD-AUTO-SMASH imaging. *Magn Reson Med* 2001;45:1066–1074.
12. Griswold MA, Jakob P, Nittka M, Goldfarb J, Haase A. Partially parallel imaging with localized sensitivities (PILS). *Magn Reson Med* 2000;44:602–609.
13. Griswold MA, Jakob PM, Heidemann RM, Nittka M, Jellus V, Wang J, Kiefer B, Haase A. Generalized autocalibrating partially parallel acquisitions (GRAPPA). *Magn Reson Med* 2002;47:1202–1210.
14. Beatty PJ. Reconstruction methods for fast magnetic resonance imaging. PhD thesis, Stanford University, 2006.

15. Griswold MA, Kannengiesser S, Heidemann R, Wang J, Jakob P. Field-of-view limitations in parallel imaging. *Magn Reson Med* 2004;52: 1118–1126.
16. Seiberlich N, Breuer F, Heidemann R, Blaimer M, Griswold MA, Jakob P. Reconstruction of undersampled non-Cartesian data sets using pseudo-Cartesian GRAPPA in conjunction with GROG. *Magn Reson Med* 2008;59:1127–1137.
17. Heidemann R, Griswold MA, Seiberlich N, Krüger G, Kannengiesser S, Kiefer B, Wiggins G, Wald L, Jakob P. Direct parallel image reconstructions for spiral trajectories using GRAPPA. *Magn Reson Med* 2006;56:317–326.
18. Heberlein K, Hu X. Auto-calibrated parallel spiral imaging. *Magn Reson Med* 2006;55:619–625.
19. Hu P, Meyer CH. Bosco: parallel image reconstruction based on successive convolution operations. In: *Proceedings of the 14th Annual Meeting of ISMRM*, Seattle, 2006. p 10.
20. Jackson JI, Meyer CH, Nishimura DG, Macovski A. Selection of a convolution function for Fourier inversion using gridding. *IEEE Trans Med Imaging* 1991;10:473–478.
21. Beatty PJ, Nishimura DG, Pauly JM. Rapid gridding reconstruction with a minimal oversampling ratio. *IEEE Trans Med Imaging* 2005;24: 799–808.
22. Fessler J, Sutton B. Nonuniform fast fourier transforms using min-max interpolation. *IEEE Trans Signal Processing* 2003;51:560–574.
23. Man L, Pauly JM, Macovski A. Multifrequency interpolation for fast off-resonance correction. *Magn Reson Med* 1997;37:785–792.
24. Sutton B, Noll D, Fessler J. Fast, iterative image reconstruction for MRI in the presence of field inhomogeneities. *IEEE Trans Med Imaging* 2003;22:178–188.
25. Lustig M, Donoho DL, Pauly JM. Sparse MRI: the application of compressed sensing for rapid MR imaging. *Magn Reson Med* 2007;58: 1182–1195.
26. Buckheit J, Donoho DL. Wavelab and reproducible research. In: Antoniadis A, ed., *Wavelets and statistics*, Germany: Springer-Verlag; 1996, pp 55–81.
27. Paige CC, Saunders MA. LSQR: An algorithm for sparse linear equations and sparse least-squares. *TOMS* 1982;8:43–71.
28. Donoho DL, Maleki A, Shahram M, Stodden V, Rahman I. 15 Years of reproducible research in computational harmonic analysis. Technical Report, Stanford University, 2008; P 02.
29. Lustig M, Alley MT, Vasanawala S, Donoho DL, Pauly JM.  $\ell_1$ -Spirit: autocalibrating parallel imaging compressed sensing. In: *Proceedings of the 17th Annual Meeting of ISMRM*, Honolulu, HI, 2009. p 379.
30. Santos JM, Wright G, Pauly JM. Flexible real-time magnetic resonance imaging framework. *Conf Proc IEEE Eng Med Biol Soc* 2004;2: 1048–1051.
31. Samsonov A. On the optimality of parallel MRI in  $k$ -space. *Magn Reson Med* 2008;59:156–164.